THE JOURNAL OF PHYSICAL CHEMISTRY C

Subscriber access provided by UNIVERSITY OF TOLEDO LIBRARIES

C: Surfaces, Interfaces, Porous Materials, and Catalysis

Iron-Based Perovskites for Catalyzing Oxygen Evolution Reaction

Binghong Han, Alexis Grimaud, Livia Giordano, Wesley T. Hong, Oscar Diaz-Morales, Yueh-Lin Lee, Jonathan Hwang, Nenian Charles, Kelsey A. Stoerzinger, Wanli Yang, Marc T.M. Koper, and Yang Shao-Horn

J. Phys. Chem. C, **Just Accepted Manuscript** • DOI: 10.1021/acs.jpcc.8b01397 • Publication Date (Web): 29 Mar 2018

Iron-Based Perovskites for Catalyzing Oxygen Evolution Reaction

Binghong HAN[1#], Alexis GRIMAUD[2,3#], Livia GIORDANO[2,5#], Wesley T. HONG[1], Oscar DIAZ-MORALES[4], Yueh-Lin LEE[2,3], Jonathan HWANG[1], Nenian Charles[1,3], Kelsey A. Stoerzinger[1], Wanli YANG[6], Marc T.M. KOPER[7], Yang SHAO-HORN[*1,2,3]

[1]Department of Materials Science and Engineering, [2]Department of Mechanical Engineering, [3]Research Laboratory of Electronics, Massachusetts Institute of Technology, Cambridge, MA, United States

[4] Department of Physics, AlbaNova University Center, Stockholm University, S-10691 Stockholm, Sweden

[5]Dipartimento di Scienza dei Materiali, Università di Milano-Bicocca, Milano, Italy

[6]Advanced Light Source, Lawrence Berkeley National Laboratory, Berkeley, CA, United States

[7]Leiden Institute of Chemistry, Leiden University, Leiden, The Netherlands

[#]Equal contributors

Corresponding Author*

Email: shaohorn@mit.edu

Telephone: (617) 253-2259

Abstract

The slow kinetics of the oxygen evolution reaction (OER) is the main cause of energy loss in many low-temperature energy storage techniques, such as metal-air batteries and water splitting. A better understanding of both the OER mechanism and the degradation mechanism on different transition metal oxides is critical for the development of the next generation of oxides as OER catalysts. In this paper, we systematically investigated the catalytic mechanism and lifetime of $ABO_{3-\delta}$ perovskite catalysts for OER, where A = Sr or Ca and B = Fe or Co. During the OER process, the Fe-based $AFeO_{3-\delta}$ oxides with $\delta \approx 0.5$ demonstrate no activation of lattice oxygen or pH dependence of OER activity, which is different from the $SrCoO_{2.5}$ with similar oxygen 2p-band position relative to the Fermi level. The difference was attributed to the larger changes in the electronic structure during the transition from the oxygen-deficient brownmillerite structure to the fully-oxidized perovskite structure and the poor conductivity in Fe-based oxides, which hinders the uptake of oxygen from the electrolyte to the lattice under oxidative potentials. The low stability of Fe-based perovskites under OER conditions in basic electrolyte also contribute to the different OER mechanism compared with the Co-based perovskites. This work reveals the influence of transition metal composition and electronic structure on the catalytic mechanism and operational stability of perovskite OER catalysts.

1. Introduction

Developing highly active catalysts to promote the kinetics of the oxygen evolution reaction (OER) is critical to improving the efficiency of many clean-energy and environmental technologies, such as electrochemical and photoelectrochemical water splitting[1-2], regenerative fuel cells[3], and rechargeable metal-air batteries[4-6]. Among all the OER catalytic materials, perovskite non-precious-transition-metal oxides with the ABO_3 structure have attracted great interest because of their promising OER activities comparable to precious-metal oxides[3, 7-14]. Previous studies have shown that tuning the electronic structure of perovskites[13-14] such as moving the Fermi level of oxides closer to the oxygen *2p*-band center[7] via substituting divalent ions on the A-site and/or decreasing oxygen vacancy content can greatly enhance OER activity. However, having the O *2p*-band of perovskites too close to the Fermi level can lead to A-site cation leaching and to surface amorphization[7, 15-17] of oxides, as observed in $Ba_{0.5}Sr_{0.5}Co_{0.8}Fe_{0.2}O_{3-\delta}$ and $SrCo_{0.5}Fe_{0.5}O_{3-\delta}$[3, 7-8], leading to the formation of small layered metal oxide clusters during OER in basic solution, which are similar to those reported for electrodeposited oxide films[18-20]. In addition, shifting the O *2p*-band closer to the Fermi level may lead to a change from B-site metal leaching to A-site metal leaching from the ABO_3 perovskite structure during OER in a neutral electrolyte[21]. Additionally, for some perovskites that can catalyze OER in acid electrolytes such as $SrIrO_3$[22], whose O *2p*-band is close to the Fermi level[23], surface Sr (i.e. A-site) leaching can also be observed after the acidic OER process. All these observations demonstrate the close relationship between the electronic structure and the compositional stability of perovskites during the OER catalysis. Furthermore, tuning the electronic structure not only affects the OER activity and stability of the perovskite catalysts, but also determines the reaction mechanism. Recently, on-line electrochemical mass spectrometry (OLEMS) isotope measurements[24] and *ab initio* modeling[14] have revealed that increasing the Co-O covalency (i.e. reducing the energy difference of Co *3d* and O *2p* bands

in the density of states) in Co-based perovskites such as $La_{0.5}Sr_{0.5}CoO_{3-\delta}$ and $SrCoO_{3-\delta}$ can activate and enable oxygen sites within the perovskites to catalyze OER in basic solution in addition to transition metal sites that are considered active in the conventional proton-coupled electron transfer mechanism[25-26] for OER. It is proposed that oxygen vacancies left on the oxide surface from OER can be refilled subsequently by OH^- from the electrolyte and surface deprotonation from these hydroxyl groups yields surface oxygen, which can diffuse and fill oxygen vacancies in bulk for oxygen-deficient perovskites (reported previously as oxygen intercalation[24, 27-30]). In addition, these Co-based perovskites with high Co-O covalency and oxygen as active sites can exhibit pH-dependent OER activity on the reversible hydrogen electrode (RHE) scale[24], where increasing the pH of the electrolyte can promote the kinetics of surface deprotonation and thus enhance OER activity. In the case of Fe-based perovskites such as $SrFeO_{3-\delta}$, similar oxygen-deficient phases exist, however the electrochemical oxygen intercalation into $SrFeO_{3-\delta}$ at the room temperature is found more difficult than that into $SrCoO_{3-\delta}$[31]. Moreover, compared with $SrFeO_{3-\delta}$, it is found even more difficult to intercalate oxygen into $CaFeO_{3-\delta}$, resulting from a stronger Fe−O−Fe bond of the apical oxygen atoms in the FeO_6 octahedra in $CaFeO_{3-\delta}$[32]. All these discoveries imply that changing the A-site (e.g. from Sr to Ca) or the B-site (e.g. from Co to Fe) atoms in oxygen-deficient perovskites has a significant influence on the properties of oxygen vacancies in the bulk, which is closely related to the evolution of their electronic structures. However, the investigations of the electronic structure influence on the OER mechanism and operation stability in Fe-based perovskites are still missing, which is critical to understand the compositional effect on OER catalysis.

In this study, we compare the OER kinetics and stability of $Sr_xCa_{1-x}FeO_{3-\delta}$ (x = 0, 0.5 or 1) with $SrCoO_{3-\delta}$, which are Fe-based and Co-based perovskites whose fully-oxidized forms have comparable O *2p*-band center (relative to the Fermi level) and metal-oxygen (M-O)

covalency, according to density functional theory (DFT) calculations. Meanwhile, both DFT and the X-ray absorption spectroscopy (XAS) results indicate that the changes in electronic structure for the filling of oxygen vacancies are much greater in Fe-based perovskites than in Co-based ones, which provides a new explanation to the more difficult oxygen intercalation into the Fe-based perovskites. In addition, the large band gap of Fe-based perovskites with high oxygen vacancy leads to a poor conductivity that could further hinder the oxygen intercalation, which is confirmed by the electrochemical oxygen insertion on $SrFeO_{3-\delta}$ with different δ values. Compared with the fully-oxidized $SrCoO_3$, the oxygen-deficient $Sr_xCa_{1-x}FeO_{3-\delta}$ has a much larger gap between O *2p*-band center and the Fermi level, as well as weaker M-O covalency. Therefore, the strong pH dependence of OER activity observed in Co-based $SrCoO_{3-\delta}$ is missing in Fe-based $Sr_xCa_{1-x}FeO_{3-\delta}$. Additionally, OLEMS experiments demonstrate that the redox activity of lattice oxygen of $Sr_xCa_{1-x}FeO_{3-\delta}$ can hardly be activated during either oxygen electrochemical intercalation or OER processes, unlike $SrCoO_{3-\delta}$ on which obvious lattice oxygen evolution can be observed during OER. After cycling under OER conditions in the basic electrolyte, severe amorphization accompanied with A-site metal leaching is observed in $Sr_xCa_{1-x}FeO_{3-\delta}$. In contrast, $SrCoO_{3-\delta}$ shows only slight surface amorphization with almost no A-site metal loss after the OER. All these observations reveal that the B-site transition metal in perovskite oxides has a critical compositional effect on the OER mechanism and stability. This study provides deeper understandings of lattice oxygen activation, oxygen-site mechanism and degradation mechanism of perovskite oxides during OER, which is important for developing highly active and stable OER catalysts.

2. Methods

2.1 Oxides synthesis and bulk characterization

Perovskites $Sr_xCa_{1-x}FeO_{3-\delta}$ (x = 0, 0.5 and 1) and $SrCoO_{3-\delta}$ were synthesized by conventional solid-state routes[7]. Stoichiometric amounts of dehydrated $CaCO_3$, $SrCO_3$, Fe_2O_3 and Co_3O_4 were thoroughly ground and fired in air at 1000 °C for 12 h and then quickly quenched in liquid nitrogen to form the oxygen-deficient brownmillerite phase with $\delta \approx 0.5$. For $SrFeO_{3-\delta}$, the quenched products were ground and then annealed a second time in Ar, air or O_2 at 1000 °C, and then slowly cooled down to room temperature to tune the δ (i.e. to tune the oxygen vacancy) in $SrFeO_{3-\delta}$. The values of δ (i.e. the amount of oxygen vacancy) in $SrFeO_{3-\delta}$ were determined by comparing the X-ray adsorption spectra with previous references[33], as shown in Figure S1 in the Supporting Information (SI). All oxides examined in this study were single phase, as revealed by X-ray diffraction (XRD), with lattice parameters listed in Table S1 in the SI. XRD measurements were performed using a PANalytical X'Pert Pro powder diffractometer in the Bragg-Brentano geometry using Copper K_α radiation, where data were collected using the X'Celerator detector in the 8-80° window in the 2θ range. The specific surface area of each oxide sample was determined using Brunauer, Emmet and Teller (BET) analysis on a Quantachrome ChemBET Pulsar from a single-point BET analysis performed after 12 h outgassing at 150 °C (see Table S2 in the SI).

2.2 Density Functional Theory Studies

DFT calculations with the Hubbard U correction (U_{eff} = 3.3 eV for Co and 4.0 eV for Fe 3*d* electrons)[34-35] were performed with the Vienna *Ab-initio* Simulation Package (VASP)[36-37] using the Projector-Augmented plane-Wave method[38]. The metal 3*d*-band and oxygen 2*p*-band centers were determined with the same computational setup as in our previous studies[24,

[34-35]. For the analysis of the energetics and electronic structure modifications during oxygen intercalation in $SrCoO_{3-\delta}$, $SrFeO_{3-\delta}$ and $CaFeO_{3-\delta}$ ($0 \leq \delta \leq 0.5$) we used the Perdew-Burke-Ernzerhof PBE functional[39] and an energy cutoff of 500 eV. For Ca and Sr, $(n-1)s^2(n-1)p^6ns^2$ (n = 4 for Ca and 5 for Sr) were included as valence electrons, for Co $3d^7\ 4s^2$, for Fe $3d^6\ 4s^2$, and for O $2s^2 2p^4$ (standard O pseudopotential). The $ABO_{2.5}$ (A= Ca, Sr and B = Fe, Co) compounds were simulated in the I2*bm* vacancy-ordered brownmillerite structure[40] (see Figure S2). We have verified that the use of the P*bcm* structure, which is the ground state for $SrFeO_{2.5}$[41], changes the results by less than 15 meV/formula unit. $ABO_{2.75}$ and $ABO_{2.875}$ intermediate structures (A= Ca, Sr and B = Fe, Co) were adapted from Ref.[42] (see Figure S3). The P*nma* structure was used for the fully oxidized ABO_3 perovskites (Figure S2). For each oxygen content, ferromagnetic (FM) and G-type antiferromagnetic (GAFM) states were computed. The high-spin configuration was found to be stable for the Fe-compounds, while for $SrCoO_{3-\delta}$ an intermediate spin state was found to be stable for octahedral Co ions and a ferrimagnetic spin state was found for $SrCoO_{2.5}$, instead of the reported insulating G-type antiferromagnetic state[43]. A K-point sampling equivalent to (12 × 12 × 12) for the cubic perovskite unit cell was used for the $ABO_{3-\delta}$ structures.

2.3 X-ray Absorption Spectroscopy

XAS data were collected at Beamline 8.0.1 of the Advanced Light Source (Lawrence Berkeley National Laboratory). The experiments were performed with the samples at room temperature under ultra-high vacuum (UHV) conditions (10^{-9} Torr), with the linear polarization of the incident beam 45° to the sample surfaces. The O K-edge (1s to 2p) spectra were collected in total fluorescence yield (TFY).

2.4 Electrochemical measurements of OER activities

OER activity of oxide powder was measured by both cyclic voltammetry (CV) and galvanostatic measurements in a glass three-electrode cell with a Ag/AgCl reference electrode and Pt counter electrode in oxygen-saturated 0.1 M KOH (99.99% purity, Sigma Aldrich) electrolyte. The working electrode consisted of oxide, acetylene black (AB) particles and Nafion® (with a mass ratio of 5:1:1) dispersed on a glassy carbon electrode (5 mm diameter) prepared by drop casting as described previously[44]. All electrochemical measurements were done using a Biologic SP-300 potentiostat. CV measurements were performed at a scan rate of 10 mV/s and a rotation of 1600 rpm while galvanostatic measurements were performed at different current densities without rotation. The Ag/AgCl reference electrode was calibrated in the same electrolyte by measuring hydrogen oxidation/evolution using a platinum electrode and defining the point of zero current as 0 V vs. RHE. OER kinetic currents were obtained from taking the average between forward and backward scans from CV measurements to remove the capacitive current contribution, which was then corrected for ohmic losses. Ohmic losses were corrected by subtracting the ohmic voltage drop from the measured potential, using an electrolyte resistance determined by high-frequency AC impedance, where *iR*-corrected potentials are denoted as $E - iR$ (*i* as the current and *R* as the electrolyte resistance). The Tafel slope was determined from the CV and galvanostatic measurements of fully oxidized oxides that were pre-charged galvanostatically at the rate of 7.3 mA/g_{oxide} in O_2-saturated electrolyte (see Figures S4 and S5 in the SI). Error bars of the measured OER activities were taken as the standard deviation from at least 3 independent measurements. As currents in the CV measurements of pristine oxides with considerable oxygen vacancies could include bulk oxidation (i.e. $SrFeO_{3-\delta} + 2\delta OH^- \rightarrow SrFeO_3 + \delta H_2O + 2\delta e^-$ [28-29]) in addition to OER, larger oxidation currents were found from CV measurements than galvanostatic measurements.

2.5 Online Electrochemical mass spectroscopy

OLEMS experiments[45] were performed using an EvoLution mass spectrometer system (European Spectrometry systems Ltd.). The setup has a mass detector (Prisma QMS200, Pfeiffer) which was brought to vacuum using both a turbo molecular pump (TMH-071P, Pfeiffer, flow rate 60 L s^{-1}) and a rotary vane pump (Duo 2.5, Pfeiffer; flow rate 2.5 m^3 h^{-1}). During measurements, the pressure inside the mass detector chamber was around 10^{-6} mbar. Volatile reaction products were collected from the electrode interface by a small inlet tip positioned close (~ 10 μm) to the electrode surface using a micrometric screw system and a camera. The inlet tip was made with a porous Teflon cylinder (Porex) mounted in a Kel-F holder, which was connected to the mass detector through a PEEK capillary. Before use, the inlet tip was cleaned for 15 min with a solution 0.2 M $K_2Cr_2O_7$ in 2 M H_2SO_4 and rinsed thoroughly with water. The electrochemical cell used for these experiments is a two-compartment cell with three electrodes, using a gold wire as counter electrode and an RHE as reference electrode. The reference electrode was separated from the main cell by a Luggin capillary. The working electrode was prepared by drop-casting an ink containing the oxide as in the experiment described for the determination of the OER activity but using a gold disk electrode (4.6 mm diameter), and the ink used for these experiments did not contain acetylene black (AB). Before each measurement, the working electrode was electrochemically cleaned; the electrode was first oxidized in 1 M sulfuric acid by applying 10 V for 30 s, using a glassy carbon plate as the counter electrode. Subsequently the gold oxide formed was removed by dipping the working electrode in a 6 M HCl solution for 30 s and rinsed with deionized water. The electrochemically cleaned working electrode was flame annealed and cooled before drop-casting the inks. Oxygen-deficient perovskites were drop casted on the working electrode with a loading of 0.25 mg_{oxide}/cm^2_{disk} and first measured in 0.1 M KOH $H_2{}^{16}O$ electrolyte by cyclic

voltammetry between 1.2 and 1.7 V vs. RHE at 2 mV/s (2 cycles); this measurement is described in the work as pristine. After the OER measurement of the pristine electrodes, they were oxidized for 10 min in 0.1 M KOH solution prepared with ^{18}O-labeled water (GMP standard from CMR, 98% ^{18}O) at 1.6 V versus gold counter electrode, in order to label them with ^{18}O. Electrodes were then rinsed with ^{16}O water to remove $H_2{}^{18}O$ and measured in 0.1 M KOH solution of $H_2{}^{16}O$ at 2 mV/s for 2 cycles. No significant signals of m/z = 34 ($^{18}O^{16}O$) and m/z = 36 ($^{18}O/^{18}O$) were detected in the second cycle for oxides studied (Figure S6).

2.6 Transmission Electron Microscope

A JEOL 2010F Transmission Electron Microscope (TEM) equipped with the ultrahigh resolution polepiece was used to collect TEM images and energy dispersive spectroscopy (EDS) in this work, with a point resolution of 0.19 nm. The high-resolution TEM (HRTEM) images were analyzed using Gatan Digital Micrograph v2.01 (Gatan Inc.) and ImageJ v1.44p (National Institute of Health, USA). Parallel-beam EDS results were collected and analyzed using INCA (Oxford Instruments) software. For each sample, three different spots with a diameter of ~ 200 nm were used to collect the bulk chemical compositions, while three different spots with a diameter of ~ 5 nm at the particle edges were used to collect the surface chemical composition. Error bars of elemental compositions obtained from EDS data represent the standard deviation of the results on at least three spots. The oxide TEM samples were prepared by dropping the catalyst ink onto Cu grids or using grids to scratch the working electrode after OER measurements.

3. Results and Discussion

3.1 Oxygen-vacancy-dependent electronic structure for Fe-based perovskites

To study the influence of transition metal (TM) compositions on the OER kinetics and structural stability on perovskite oxides, we synthesized and investigated $Sr_xCa_{1-x}FeO_{3-\delta}$ (x = 0, 0.5 or 1) and $SrCoO_{3-\delta}$, whose fully-oxidized forms (i.e. $\delta = 0$) have comparable O *2p*-band centers (relative to the Fermi level) and M-O covalency, as shown in Figure 1. According to our previous study, when the O *2p*-band center is close enough to the Fermi level and when the M-O covalency is strong enough, like in $SrCoO_3$, the redox of lattice oxygen in the perovskite structure will be activated during the OER, leading to the evolution of lattice oxygen and the pH dependence of OER kinetics on RHE scale[24]. Therefore, from the electronic structure point of view, we would expect $SrFeO_3$ and $CaFeO_3$ to show similar redox activity of lattice oxygen during the OER process. However, in practice, the fully-oxidized $Sr_xCa_{1-x}FeO_3$ or $SrCoO_3$ are not stable under ambient conditions and cannot be directly synthesized[30, 32]. The oxygen deficiency in these perovskite oxides can lead to larger energy gaps between their O *2p*-band centers and their Fermi level, as well as weaker M-O covalencies. For example, increasing the δ value from 0 to 0.5 will separate the O *2p*-band center from the Fermi level by more than 0.8 eV and weaken the Fe-O covalency by more than 0.3 eV in $SrFeO_{3-\delta}$ and $CaFeO_{3-\delta}$, as shown in Figure 1b. Therefore, the full oxidation of perovskite oxides (i.e. the filling of oxygen vacancies) has a critical influence on the electronic structure, and can determine the OER performance and mechanism. In the case of $SrCoO_{3-\delta}$, the oxygen vacancies can be slowly filled in the electrolyte under the oxidative voltages that are lower than the OER potential[24], therefore we can assume that the OER is catalyzed on a fully-oxidized $SrCoO_3$ structure, particularly since the oxides were pre-charged galvanostatically in O_2-saturated electrolyte in our previous paper[24] and in this work. However, the filling of oxygen vacancies may not always happen prior to the OER. The

energy penalties and electronic structure rearrangements for the transformation from the $ABO_{3-\delta}$ to the fully-oxidized ABO_3 are closely related to the A and B site compositions, as shown in the discussions below.

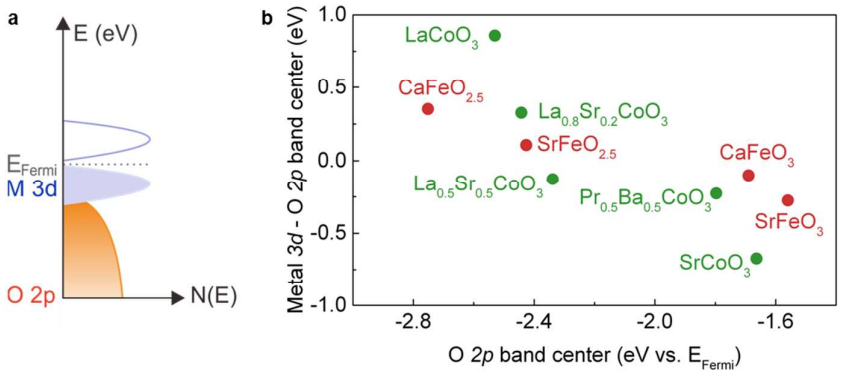

Figure 1. (a) Scheme of oxygen 2*p*-band and metal 3*d*-band for ABO_3 perovskite oxides. (b) Relative positions of the total metal 3*d*-band center and the total oxygen 2*p*-band center plotted against the oxygen 2*p*-band center for selected Co-based (green) and Fe-based (red) perovskite oxides computed at DFT+U level. Both O 2*p*-band and metal 3*d*-band centers were determined by taking the centroid of the projected density of states of O *2p* and metal *3d* states (both occupied and unoccupied states) relative to the Fermi level. The energy band calculation results of Co-based perovskites have been reported in our previous study[24].

The degree of change in the electronic structure associated with the oxygen non-stoichiometry is most transparent in the XAS measurements at the O K-edge, as shown in Figure 2a. As the oxygen non-stoichiometry changes from $\delta = 0.20$ to $\delta = 0.45$, in $SrFeO_{3-\delta}$ the O K-edge shifted by ~1.3 eV, while in $SrCoO_{3-\delta}$ the shift was below 0.4 eV. The significant oxygen band shifts observed in $SrFeO_{3-\delta}$ are consistent with our computed DOS, showing the opening of a band gap in the GAFM $SrFeO_{2.5}$ (Figure 2e). The shift also agrees with previous studies showing the bands in $La_{1-x}Sr_xFeO_{3-\delta}$ are highly non-rigid[46]. In contrast, only slight shifts in O

K-edge are observed in the XAS spectra for $SrCoO_{3-\delta}$ when varying δ, demonstrating a near-rigid behavior, similarly to $La_{1-x}Sr_xCoO_{3-\delta}$.[47] This is consistent with the small changes observed in the computed DOS (Figure 2d). The magnitude of the pre-edge shift is due to the change in TM electron density and metal-oxygen hybridization associated with the nominally Fe^{3+}/Fe^{4+} and Co^{3+}/Co^{4+} redox couples. Actually, previous study has shown that the lineshape change for the XAS spectra at the O K-edge in these TM oxides mostly corresponds to the changes of TM states[48]. The pre-edge shift suggests that larger changes in the electronic structure are needed to transit between Fe^{3+}/Fe^{4+} than between Co^{3+}/Co^{4+} in perovskite oxides, which is also evident from the TM *L*-edge XAS spectra (Figure 2b): as the oxygen vacancy concentration increases, more substantial changes appear in the Fe *L*-edge than what has been reported for the Co *L*-edge.[49] Because the O *K*-edge and TM *L*-edge positions of $SrCoO_{3-\delta}$ are nearly identical in samples with different δ values, the kinetic penalty for changing the oxygen stoichiometry (i.e. oxygen intercalation) is expected to be small. In contrast, the larger changes in both O *K*-edge and TM *L*-edge positions for $SrFeO_{3-\delta}$ as a function of oxygen vacancy content δ indicate a much larger kinetic penalty for filling oxygen vacancies compared to $SrCoO_{3-\delta}$. Thus, although $SrFeO_{3-\delta}$ and $SrCoO_{3-\delta}$ are both well-known charge-transfer oxides,[50] their redox properties differ quite drastically because the Fe^{3+}/Fe^{4+} transition results in a more localized charge density on the TM atom than the Co^{3+}/Co^{4+} transition[51]. The difficulty to intercalate lattice oxygen in $SrFeO_{3-\delta}$, $CaFeO_{3-\delta}$ and $SrCoO_{3-\delta}$ can also be measured by the changes in electronic structures and the energetics of phase transformation from the antiferromagnetic $SrMO_{2.5}$ brownmillerite structure to the ferromagnetic ABO_3 (A = Ca and Sr; B = Fe and Co) perovskite, calculated by DFT+U. The vacancy-ordered phase brownmillerite consists of alternating oxygen-deficient and fully oxidized layers, with the transition metals distributed within the octahedral sites in the fully oxidized layers and tetrahedral site in oxygen deficient layers (Figure S2), implying that the oxygen vacancy

filling in this structure requires large structural and electronic rearrangements. As shown in Figure 2c, the energy required for oxygen intercalation follows the order $CaFeO_{3-\delta}$ > $SrCoO_{3-\delta}$ > $SrFeO_{3-\delta}$. However, the energy requirement may not be the only factor that determines the ability to fill oxygen vacancies during the electrochemical oxidation process for these perovskite compounds. Indeed, we note that for $CaFeO_{3-\delta}$, $SrCoO_{3-\delta}$, and $SrFeO_{3-\delta}$, an AFM-FM transition always occurs during oxygen intercalation. Particularly, the two Fe compounds ($CaFeO_{3-\delta}$ and $SrFeO_{3-\delta}$) display stronger magnetic coupling than $SrCoO_{3-\delta}$ (Figure S7). Therefore, despite the thermodynamics for oxidation being more favorable for $SrFeO_{3-\delta}$, the extensive changes in both the measured (Figures 2a-b) and calculated (Figures 2d-f) electronic structures point towards a more difficult filling of oxygen vacancies in $SrFeO_{3-\delta}$ and $CaFeO_{3-\delta}$ than in $SrCoO_{3-\delta}$. In addition, the large band gap of $SrFeO_{2.5}$ and $CaFeO_{3-\delta}$ observed in the calculated DOS suggests a poor electrical conductivity, which may also lead to a more difficult electrochemical oxygen insertion compared with the fairly conductive $SrCoO_{2.5}$.

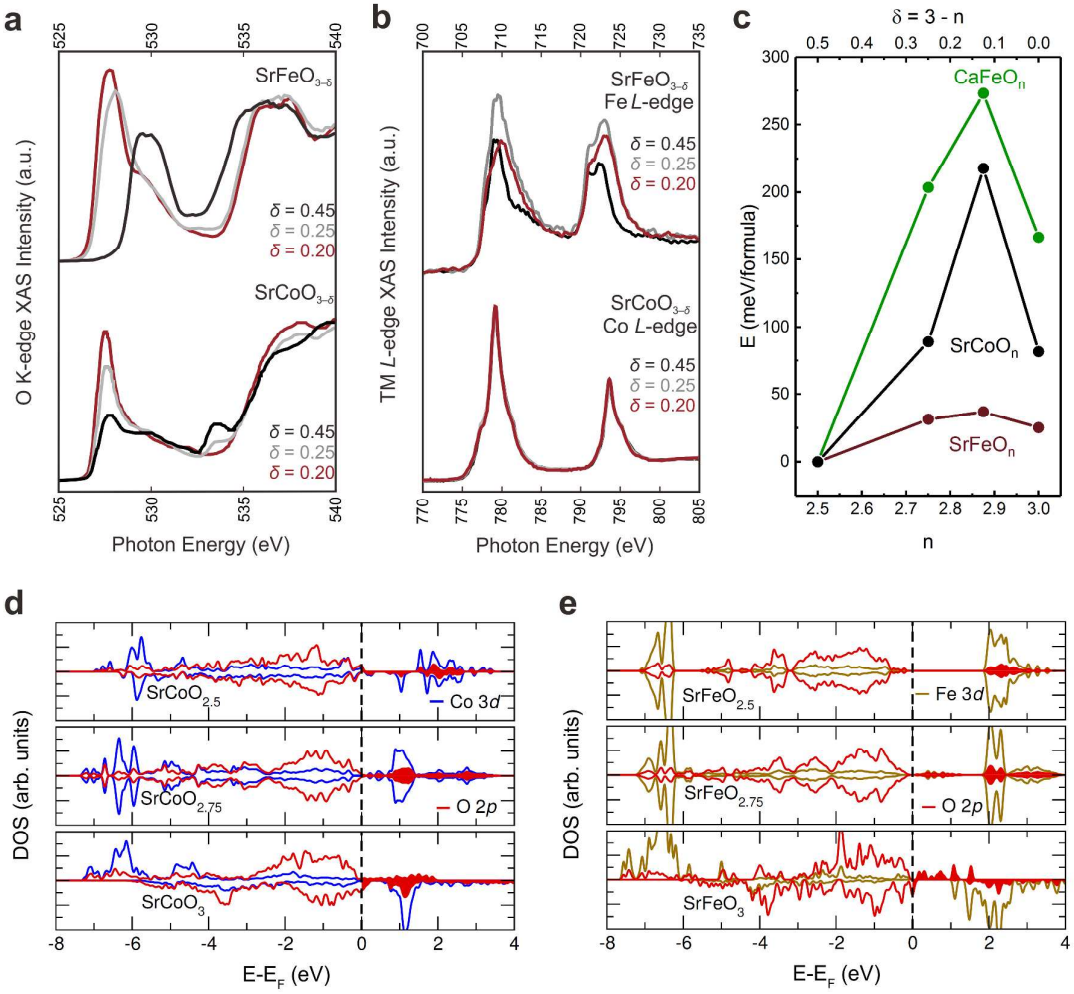

Figure 2. (a) O K-edge XAS (total fluorescence yield) of $SrFeO_{3-\delta}$ measured in this study and $SrCoO_{3-\delta}$ adapted from previous work.[49] (b) Fe L-edge XAS (total fluorescence yield) of $SrFeO_{3-\delta}$ and Co L-edge XAS (total fluorescence yield) of $SrCoO_{3-\delta}$ from previous work.[49] (c) DFT+U-computed energetics of phase transformation from the $ABO_{2.5}$ (A = Ca and Sr; B = Fe and Co) brownmillerite structure (space group I2*bm*) to the ABO_3 perovskite structure (space group P*nma*). The energies of the ABO_n ($n = 3-\delta$) phases are computed as $E(ABO_{3-\delta}) + \delta\, E(O)$ and the brownmillerite structure was taken as reference, where E(O) is the energy of the H_2O to H_2 oxidation reaction at 1.23 V vs. RHE. For each n, the most energetically stable magnetic structure is reported (see Figure S7 for details). (d-e) Density of States (DOS)

projected on metal 3*d* and oxygen 2*p* states of $SrCoO_{3-\delta}$ and $SrFeO_{3-\delta}$ as a function of δ in the most stable magnetic state. The DOS of $CaFeO_{3-\delta}$ was reported in Figure S8.

3.2 Oxygen intercalation in Fe-based perovskites

To confirm the influence of the electronic structure on the actual filling of oxygen vacancies, oxygen intercalation experiments were performed on selected perovskites in O_2-saturated 1 M KOH electrolyte with a small galvanostatic current of 29.2 mA/g_{oxide} (Figure 3). Figure 3a shows the galvanostatic oxidation of $SrFeO_{3-\delta}$ ($SrFeO_{3-\delta} + 2\delta OH^- \rightarrow SrFeO_3 + \delta H_2O + 2\delta e^-$) for two oxygen nonstoichiometry value of $\delta = 0.2$ and 0.45 (obtained by annealing $SrFeO_{3-\delta}$ in O_2 and Ar, respectively). Having an oxygen vacancy content of $\delta = 0.2$, the potential of $SrFeO_{3-\delta}$ first reach a plateau at ~1.2 V vs. RHE before the onset of OER at potentials greater than ~1.4 V vs. RHE. This potential plateau before the reaching of OER potential results from the oxygen intercalation in $SrFeO_{2.8}$ to form $SrFeO_3$, where oxygen vacancies are filled in bulk[29]. However, in $SrFeO_{3-\delta}$ with an oxygen vacancies of $\delta = 0.45$, only a limited degree of oxygen intercalation is observed. Rather, the electrochemical oxidation potentials of $SrFeO_{3-\delta}$ increase significantly over 1.4 V vs. RHE enabling OER, where limited oxygen intercalation occurred. As discussed in the previous section, the more difficult oxygen intercalation in $SrFeO_{3-\delta}$ when δ is high (e.g. $\delta = 0.45$) can be attributed to the slower kinetics for oxygen vacancy filling in the antiferromagnetic brownmillerite $SrFeO_{3-\delta}$ than that in the ferromagnetic perovskite structure. For the same reason, when $SrFeO_{3-\delta}$ is pre-oxidized from the brownmillerite structure to the perovskite structure, there will be no additional kinetics penalty for the magnetic phase transformation. Therefore, the further filling of oxygen vacancies starting from the O_2-annealed $SrFeO_{3-\delta}$ with initial $\delta = 0.2$ is much easier, as shown in Figure 3a. In addition, the poor conductivity caused by the large band gap when the δ in $SrFeO_{3-\delta}$ is close to 0.5 (see Figure 2e) can also make the electrochemical oxygen insertion

more difficult. In contrast, oxygen intercalation kinetics in $SrCoO_{3-\delta}$ and $SrCo_{0.5}Fe_{0.5}O_{3-\delta}$ were found much easier even under the brownmillerite phase with high oxygen deficiency ($\delta > 0.4$, estimated by the maximum number of oxygen that can be inserted into the bulk structure at a slower charging rate of 7.3 mA/g_{oxide} reported in the previous study[24]), as shown in Figure 3b. The more difficult oxygen intercalation in $SrFeO_{3-\delta}$ than in $SrCoFeO_{3-\delta}$ has been observed in previous work[31], which was attributed to the formation of intermediates with only local and short-range ordering in $SrFeO_{3-\delta}$ during the oxygen intercalation process.

In addition to the change of the B-site cation in perovskite oxides, here we also changed the A-site in $Sr_xCa_{1-x}FeO_{3-\delta}$ (x = 0.5, 0.75 or 1), as shown in Figure 3c, and found that when Sr was gradually replaced by Ca, the oxygen intercalation became harder (illustrated by the lack of a plateau at voltages < 1.4 V vs RHE). Less oxygen can be inserted into the lattice of $Sr_xCa_{1-x}FeO_{3-\delta}$ before OER when x is smaller, consistent with a previous study[32] that attributed this behavior to the reduced Fe−O−Fe bond distance in the FeO_6 octahedra. Such an explanation is also consistent with our discussion in the earlier DFT section from the viewpoint of the electronic structures: changing the A site from Sr to Ca weakens the O-Fe hybridization and shifts the Fermi level away from the O 2*p*-band center (see Figure 1b), which makes it more difficult to oxidize the lattice before oxidizing water (OER). The influence of the A-site metal on the electronic structure can also be demonstrated by the O *K*-edge spectra measured by XAS, as shown in Figure S9. The replacement of Sr by Ca increases the O *K*-edge by more than 1.4 eV and enlarges the gap between O *2p* bands and Fermi levels, making it harder to fill the oxygen vacancies in $CaFeO_{3-\delta}$.

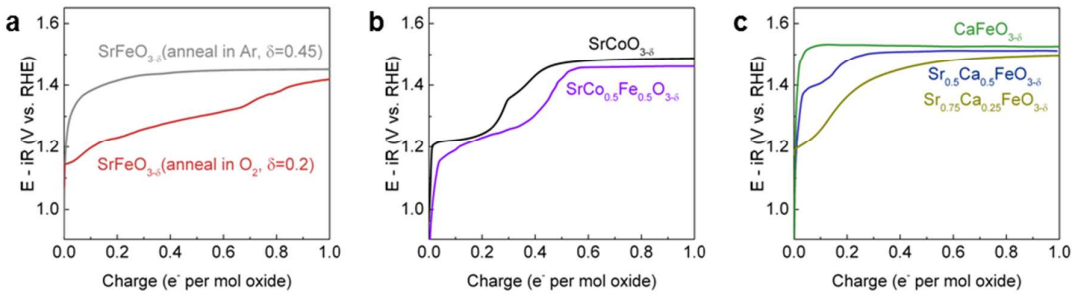

Figure 3. (a) Oxygen intercalation voltage profiles of $SrFeO_{3-\delta}$ annealed in Ar or O_2 with δ = 0.45 and 0.2, in the O_2-saturated 1 M KOH electrolyte at a charging current of 29.2 mA/g_{oxide}. (b) Oxygen intercalation voltage profiles of the quenched $SrCo_{0.5}Fe_{0.5}O_{3-\delta}$, and $SrCoO_{3-\delta}$ with initial $\delta \approx 0.5$ in the O_2-saturated 1 M KOH electrolyte at a charging current of 29.2 mA/g_{oxide}. (c) Oxygen intercalation voltage profiles of the quenched $Sr_xCa_{1-x}FeO_{3-\delta}$ (x = 0.5, 0.75 or 1, with initial $\delta \approx 0.5$) in O_2-saturated 1 M KOH electrolyte at a charging current of 29.2 mA/g_{oxide}.

3.3. OER activity of (Sr,Ca)$FeO_{3-\delta}$ and $SrCoO_{3-\delta}$

As discussed in the above section, the oxygen intercalation prior to OER can be done for $SrCoO_{3-\delta}$ but not for the highly-oxygen-deficient $Sr_xCa_{1-x}FeO_{3-\delta}$, due to their different energy and kinetics penalties for the filling of oxygen vacancies. Therefore, we would expect a much larger gap between the O *2p*-band center and the Fermi level in the oxygen-deficient $Sr_xCa_{1-x}FeO_{3-\delta}$ during the OER process. To explore how the differences in electronic structures between the fully-oxidized $SrCoO_3$ and the oxygen-deficient $Sr_xCa_{1-x}FeO_{3-\delta}$ would influence the OER kinetics and mechanisms, we measured their OER activities in KOH electrolyte at various pH values (from 12.5 to 14) by CV, potentiostatic and galvanostatic methods, as shown in Figures 4, S4 and S5. The oxides were galvanostatically pre-charged at the rate of 7.3 mA/g_{oxide} in O_2-saturated electrolyte before the OER to maximize the oxygen content. For

$SrCoO_{3-\delta}$, the OER current at the same potential on the RHE scale increases at higher pH (with reaction order with respect to protons > 70 decade/pH), while for $Sr_xCa_{1-x}FeO_{3-\delta}$ the OER activities hardly change under different pH (with reaction order < 0.15 decade/pH), implying different OER mechanisms between $Sr_xCa_{1-x}FeO_{3-\delta}$ and $SrCoO_{3-\delta}$. The strong pH-dependence of the OER activity on $SrCoO_{3-\delta}$ has been reported in our previous study, which is shown to be related to the non-concerted proton-electron transfer processes with lattice oxygen being the active site[24]. In contrast, $Sr_xCa_{1-x}FeO_{3-\delta}$ exhibits the non-pH dependent OER activity, suggesting that the OER mechanism on $Sr_xCa_{1-x}FeO_{3-\delta}$ follows the classic concerted proton-electron transfer processes. The pH independence of the OER activities on those Fe-based perovskites demonstrates that the electronic structure has a determinant influence on the oxygen content, which in turns shows great impact to the catalytic mechanism of oxide catalysts.

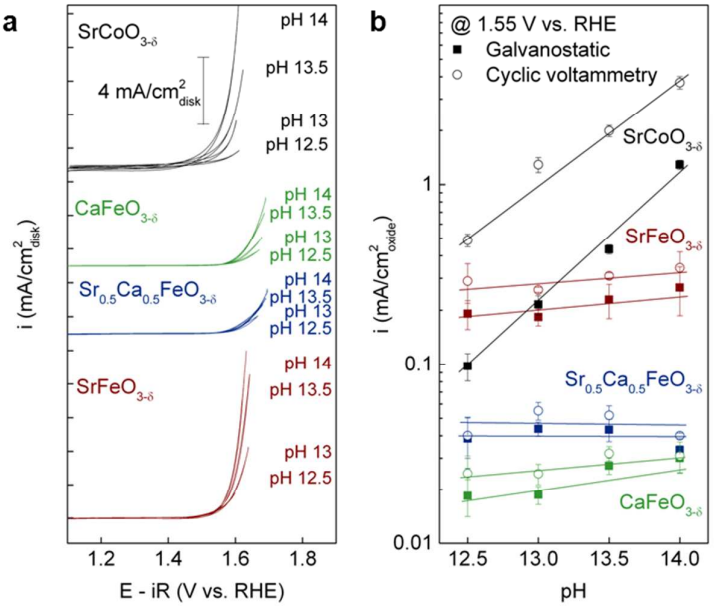

Figure 4. (a) CV measurements of $Sr_xCa_{1-x}FeO_{3-\delta}$ (x = 0, 0.5 or 1) and $SrCoO_{3-\delta}$ from O_2-saturated 0.03 M KOH (pH = 12.5) to 1 M KOH (pH = 14) recorded at 10 mV/s. (b) Specific OER activity (current normalized by oxide BET surface area) at 1.55 V vs. RHE after iR correction as a function of the pH. The nominal oxide loading is 0.25 mg_{oxide}/cm^2_{disk} and specific OER activity with error bars are given in Figures S4 and S5 in the SI. All the samples here were firstly quenched to form the $ABO_{2.5}$ compounds with $\delta \approx 0.5$. Then the oxides were galvanostatically pre-charged at the rate of 7.3 mA/g_{oxide} in O_2-saturated electrolyte before the OER. The high current from CV measurements compared with galvanostatic results could be caused by double-layer and charging current when the voltage is swept fast. The OER activity data of $SrCoO_{3-\delta}$ has been reported in our previous study[24].

3.4 OLEMS measurements of ^{18}O-labeled Fe-based perovskites

To further examine the influence of TM compositions and the corresponding electronic structures on the OER mechanisms, we performed OLEMS measurements, as described below. First, $SrCoO_{3-\delta}$ and $Sr_xCa_{1-x}FeO_{3-\delta}$ were dispersed on a gold disk electrode and labeled with ^{18}O by potentiostatic oxidation at 1.6 V vs Au in $H_2{}^{18}O$-labeled 0.1 M KOH solution. Subsequently, the electrodes were thoroughly rinsed with ^{16}O water and were measured by cyclic voltammetry (CV) scan at 2 mV/s in 0.1 M KOH-^{16}O water electrolyte while the molecular mass of evolved O_2 gas was monitored *in situ* by OLEMS. The signal for mass-to-charge ratio m/z = 32 represents $^{32}O_2$ ($^{16}O^{16}O$), m/z = 34 represents $^{34}O_2$ ($^{16}O^{18}O$), and m/z = 36 represents $^{36}O_2$ ($^{18}O^{18}O$). Figure 5a shows the signal of m/z = 36 collected from the OER in the first CV cycle, and Figure 5b shows the signal ratio between m/z = 34 and m/z = 32 to account for the natural isotopic abundance (~ 0.2%). From Figure 5 we can find that both $^{18}O^{18}O$ and $^{16}O^{18}O$ signals were detected during the OER on $SrCoO_{3-\delta}$, which was already reported in our previous study[24]. However for $Sr_xCa_{1-x}FeO_{3-\delta}$, there was no $^{18}O^{18}O$ nor $^{16}O^{18}O$

formed from lattice oxygen during OER, indicating that the redox activity of their lattice oxygen is not activated for OER. This again is because $Sr_xCa_{1-x}FeO_{3-\delta}$ cannot be fully oxidized before the OER, leading to a larger gap between the O 2*p*-band and the Fermi level, which makes it energetically more difficult to oxidize the lattice oxygen during the OER process. Therefore, the OER catalysis only occurs on the metal sites following the traditional proton-electron coupled mechanistic routes, and the lattice oxygen is not evolved during the OER, which is indicated by the lack of ^{18}O-labeled lattice oxygen evolution detected by the OLEMS tests. Furthermore, the non-activated lattice oxygen observed on $Sr_xCa_{1-x}FeO_{3-\delta}$ is consistent with their pH-independent OER activities discussed in the previous section.

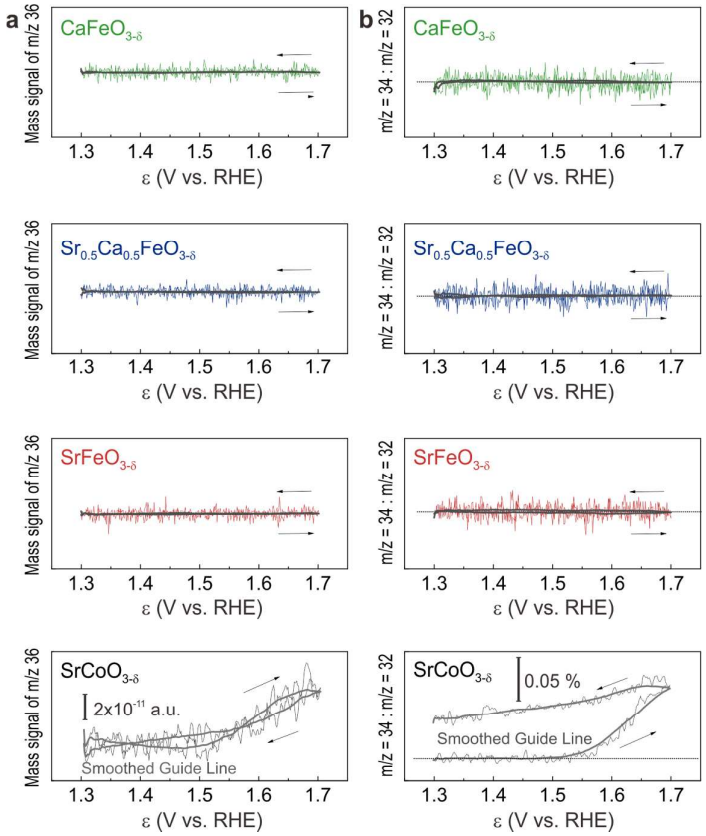

Figure 5. (a) $^{36}O_2$ gas signal and (b) $^{34}O_2$ / $^{32}O_2$ signal ratio measured by OLEMS for ^{18}O-labeled $Sr_xCa_{1-x}FeO_{3-\delta}$ (x = 0, 0.5 or 1) and $SrCoO_{3-\delta}$, which were taken from the first cyclic

voltammetry scan. All the samples here were first quenched to form the $ABO_{2.5}$ compounds with $\delta \approx 0.5$. Then the oxides were oxidized in 0.1 M KOH made with ^{18}O-labeled water (GMP standard from CMR, 98% ^{18}O) at 1.6 V vs. gold counter electrode for 10 min (no gas bubbling), in order to label with ^{18}O. The straight dashed lines in (b) correspond to the natural abundance of ^{18}O of 0.2%. The arrows indicate the directions of positive and negative scans. The OLEMS data in the first and second CV cycles can be found in Figure S6. The OLEMS data of $SrCoO_{3-\delta}$ has been reported in our previous study[24].

3.5 Instability of Fe-based perovskites during OER

The change of TM compositions and the electronic structures in perovskite oxides not only affect the OER kinetics, but also influence the stability during the OER. The HRTEM images and the EDS results of $Sr_xCa_{1-x}FeO_{3-\delta}$ (x = 0, 0.5 or 1) and $SrCoO_{3-\delta}$ samples before and after the OER CV measurements are shown in Figure 6. Before OER, all oxide particles exhibit sharp lattice fringes extending to the particle surfaces. Moreover, the bulk and surface element ratios between A-site (Ca and/or Sr) and B-site (Fe or Co) metals are all around 1 as expected from the nominal stoichiometry. After the OER CV measurements, $Sr_xCa_{1-x}FeO_{3-\delta}$ particles showed surface amorphization with thicknesses on the order of 5-10 nm, accompanied with severe leaching of surface A-site (i.e. Sr and/or Ca), as deduced by the EDS analysis. Similar A-site metal leaching after OER has been observed at neutral pH [21] and low pH [22]. In contrast, $SrCoO_{3-\delta}$ exhibits less visible surface structural changes and its surface metal ratios remained unchanged after OER. The stability of surface structures can also influence the stability of OER kinetics. As shown in Figure S10, when holding the current at 0.2 mA/cm^2_{oxide}, the potential on $SrCoO_{3-\delta}$ gradually stabilized after the initial fluctuation related to the double-layer capacity, while the potential for $Sr_xCa_{1-x}FeO_{3-\delta}$ dropped quickly over time due to the continuous surface amorphization. Similar activity change caused by the surface

amorphization has been previously observed in $Ba_{0.5}Sr_{0.5}Co_{0.8}Fe_{0.2}O_{3-\delta}$[3, 8]. The fast OER activity dropping over CV cycles has also been observed on $La_xSr_{1-x}FeO_{3-\delta}$, where less surface oxygen vacancy is correlated with stronger activity loss[52]. Actually, the severe amorphization of $Sr_xCa_{1-x}FeO_{3-\delta}$ observed in this paper may also prevent its full oxidation into $Sr_xCa_{1-x}FeO_3$ under the OER potential, which leads to larger gap between its O 2*p*-band and Fermi level (see Figure 1b), hinders the activation of lattice oxygen during OER, and results in a pH-independent OER activity with no evolution of lattice oxygen during the OER. Nevertheless, the notable stability difference between $SrCoO_{3-\delta}$ and $Sr_xCa_{1-x}FeO_{3-\delta}$ is not fully understood yet and requires further investigations.

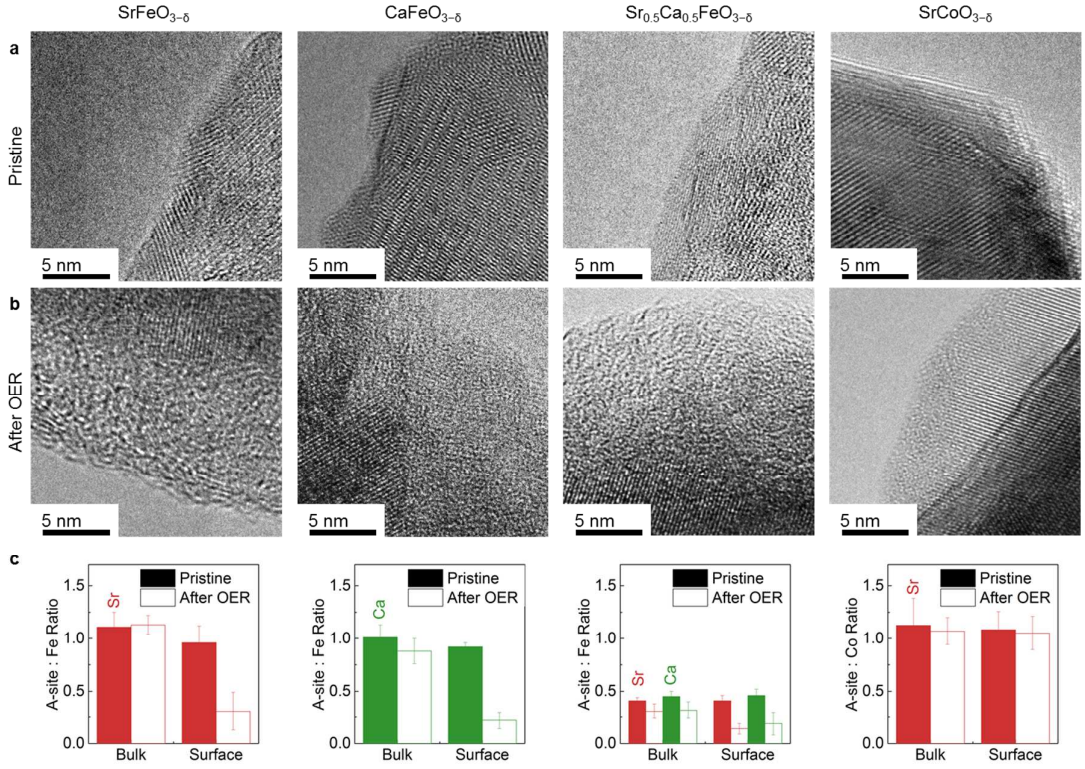

Figure 6. HRTEM images and EDS results of $Sr_xCa_{1-x}FeO_{3-\delta}$ (x = 0, 0.5 or 1) and $SrCoO_{3-\delta}$. (a) HRTEM images of pristine powder. (b) HRTEM images of oxide surfaces after OER in the CV measurements shown in Figure 4 (measured under 4 different pH values for 12 CV cycles total). (c) The bulk and surface A-site and B-site metal ratios before and after OER

measurements as determined by EDS. The error bars in (c) represent the standard deviation of at least three spots. All the pristine oxides here were quenched to form the $ABO_{2.5}$ compounds with $\delta \approx 0.5$.

3.6 Compositional effect on the OER mechanism and structural stability of perovskites

For $SrCoO_{3-\delta}$, we observe strong pH dependence of OER activity and detect the evolution of lattice oxygen during the OER process using OLEMS, which suggested the non-concerted proton-electron transfer processes with lattice oxygen being the active site[24]. However, in $Sr_xCa_{1-x}FeO_{3-\delta}$, the OER activity shows no pH dependence and the OLEMS data demonstrates no lattice oxygen evolving during OER. Therefore it is likely that the OER on $Sr_xCa_{1-x}FeO_{3-\delta}$ follows the classic metal-site mechanism, which is similar to $LaCoO_3$ in the previous OLEMS study[24]. However, unlike $LaCoO_3$ whose lattice oxygen is not activated due to a large gap between the O 2p-band center and the Fermi level, the DFT results in Figure 1b show that the energy gap between the O 2*p*-band center and the Fermi level in the fully oxidized $Sr_xCa_{1-x}FeO_3$ is as small as that in $SrCoO_3$. Therefore, thermodynamically the lattice oxygen in $Sr_xCa_{1-x}FeO_3$ should be as easily activated during the OER as in $SrCoO_3$. The fact that the activation of lattice oxygen during OER observed for $SrCoO_{3-\delta}$ is absent on $Sr_xCa_{1-x}FeO_{3-\delta}$ indicates that the full oxidation of the structure is hindered. The XAS and DFT results indicate that a large electronic structure changes are required in Fe-based perovskites for the phase transformation from the high-oxygen-deficient brownmillerite structure to the low-oxygen-deficient perovskite structure, which can affect the oxygen insertion and prevent the full oxidation of the Fe-based perovskites before the OER. The poor conductivity of $SrFeO_{3-\delta}$ with δ close to 0.5 could further hinder the electrochemical oxygen intercalation process. In addition, the TEM and EDS characterizations demonstrate the A-site metal leaching and the thick amorphous layer formation on Fe-based perovskites, giving another explanation to the missing of lattice oxygen activation. In both hypotheses, the B-site TM composition exhibits

great influence on the evolution of atomic and electronic structures during OER, and therefore leads to different OER mechanisms and kinetics. In general, we find that changing the B-site from Co to Fe in the $ABO_{3-\delta}$ oxides leads to very different oxygen deficiency conditions, stability issues, and OER mechanisms to the OER catalysis. Therefore Fe-based perovskites should not be simply analogized to or compared with Co-based perovskites for OER catalysis only based on their similar electronic structures.

Conclusion

In conclusion, by combining experimental characterizations with theoretical simulations, we demonstrate that the B-site transition metal has a critical influence on the evolution of the atomic and electronic structures of perovskite oxides during the OER catalysis. The Fe-based perovskites show a more difficult oxygen intercalation before OER and a greater surface amorphization during OER, which can prevent the activation of lattice oxygen and lead to a change of OER mechanism. These new findings provide deeper insights into the selection of transition metals to tailor the bulk electronic structure of oxide catalysts, the resulting OER mechanism, and the stability of the oxide catalysts.

AUTHOR INFORMATION

Corresponding Author

*E-mail: shaohorn@mit.edu

Notes

The authors declare no competing financial interest.

ASSOCIATED CONTENT

Supporting Information

The Supporting Information is available free of charge on the ACS Publications website: tables for basic material properties, structural model for DFT calculations, additional electrochemical test, OLEMS, XAS, and DFT results.

ACKNOWLEDGMENTS

This work was supported in part by the Skoltech-MIT Center for Electrochemical Energy, the SMART program, the Department of Energy (DOE) and National Energy Technology Laboratory (NETL), Solid State Energy Conversion Alliance (SECA) Core Technology Program (Funding Opportunity Number DEFE0009435). This work is also supported in part by the Netherlands Organization for Scientific Research (NWO) within the research program of BioSolar Cells, co-financed by the Dutch Ministry of Economic Affairs, Agriculture and Innovation. Authors thank Ruimin Qiao for guidance with the XAS measurements. The Advanced Light Source is supported by the Director, Office of Science, Office of Basic Energy Sciences, of the U.S. Department of Energy under Contract No. DE-AC02-05CH11231. This research used resources of the National Energy Research Scientific Computing Center, a DOE Office of Science User Facility supported by the Office of Science of the U.S. Department of Energy under Contract No. DE-AC02-05CH11231. This work also used resources of the Extreme Science and Engineering Discovery Environment (XSEDE), which is supported by National Science Foundation grant number ACI-1548562.

REFERENCES

1. Lewis, N. S.; Nocera, D. G., Powering the Planet: Chemical Challenges in Solar Energy Utilization. *P. Natl. Acad. Sci.* **2006**, *103*, 15729-15735.

2. Gray, H. B., Powering the Planet With Solar Fuel. *Nat. Chem.* **2009**, *1*, 7-7.
3. Risch, M.; Stoerzinger, K. A.; Maruyama, S.; Hong, W. T.; Takeuchi, I.; Shao-Horn, Y., $La_{0.8}Sr_{0.2}MnO_{3-\delta}$ Decorated with $Ba_{0.5}Sr_{0.5}Co_{0.8}Fe_{0.2}O_{3-\delta}$: A Bifunctional Surface for Oxygen Electrocatalysis with Enhanced Stability and Activity. *J. Am. Chem. Soc.* **2014**, *136*, 5229-5232.
4. Sathiya, M., et al., Reversible Anionic Redox Chemistry in High-Capacity Layered-Oxide Electrodes. *Nat. Mater.* **2013**, *12*, 827-835.
5. Lu, Y.-C.; Gallant, B. M.; Kwabi, D. G.; Harding, J. R.; Mitchell, R. R.; Whittingham, M. S.; Shao-Horn, Y., Lithium-Oxygen Batteries: Bridging Mechanistic Understanding and Battery Performance. *Energ. Environ. Sci.* **2013**, *6*, 750-768.
6. Kwabi, D. G.; Ortiz-Vitoriano, N.; Freunberger, S. A.; Chen, Y.; Imanishi, N.; Bruce, P. G.; Shao-Horn, Y., Materials Challenges in Rechargeable Lithium-Air Batteries. *MRS Bull.* **2014**, *39*, 443-452.
7. Grimaud, A.; May, K. J.; Carlton, C. E.; Lee, Y.-L.; Risch, M.; Hong, W. T.; Zhou, J.; Shao-Horn, Y., Double Perovskites as a Family of Highly Active Catalysts for Oxygen Evolution in Alkaline Solution. *Nat. Commun.* **2013**, *4*, 2439 1-7.
8. Suntivich, J.; May, K. J.; Gasteiger, H. A.; Goodenough, J. B.; Shao-Horn, Y., A Perovskite Oxide Optimized for Oxygen Evolution Catalysis from Molecular Orbital Principles. *Science* **2011**, *334*, 1383-1385.
9. Meadowcroft, D. B., Low-cost Oxygen Electrode Material. *Nature* **1970**, *226*, 847-848.
10. Rincón, R. A.; Ventosa, E.; Tietz, F.; Masa, J.; Seisel, S.; Kuznetsov, V.; Schuhmann, W., Evaluation of Perovskites as Electrocatalysts for the Oxygen Evolution Reaction. *Chem. Phys. Chem.* **2014**, *15*, 2810-2816.
11. Hong, W. T.; Risch, M.; Stoerzinger, K. A.; Grimaud, A.; Suntivich, J.; Shao-Horn, Y., Toward the Rational Design of Non-Precious Transition Metal Oxides for Oxygen Electrocatalysis. *Energ. Environ. Sci.* **2015**, *8*, 1404-1427.
12. Hong, W. T.; Stoerzinger, K. A.; Lee, Y.-L.; Giordano, L.; Grimaud, A.; Johnson, A. M.; Hwang, J.; Crumlin, E. J.; Yang, W.; Shao-Horn, Y., Charge-Transfer-Energy-Dependent Oxygen Evolution Reaction Mechanisms for Perovskite Oxides. *Energ. Environ. Sci.* **2017**, *10*, 2190-2200.
13. Cheng, X.; Fabbri, E.; Nachtegaal, M.; Castelli, I. E.; El Kazzi, M.; Haumont, R.; Marzari, N.; Schmidt, T. J., Oxygen Evolution Reaction on $La_{1-x}Sr_xCoO_3$ Perovskites: A Combined Experimental and Theoretical Study of Their Structural, Electronic, and Electrochemical Properties. *Chem. Mater.* **2015**, *27*, 7662-7672.
14. Mefford, J. T.; Rong, X.; Abakumov, A. M.; Hardin, W. G.; Dai, S.; Kolpak, A. M.; Johnston, K. P.; Stevenson, K. J., Water Electrolysis on $La_{1-x}Sr_xCoO_{3-\delta}$ Perovskite Electrocatalysts. *Nat. Commun.* **2016**, *7*, 11053.
15. Hua, B.; Sun, Y.-F.; Li, M.; Yan, N.; Chen, J.; Zhang, Y.-Q.; Zeng, Y.; Shalchi Amirkhiz, B.; Luo, J.-L., Stabilizing Double Perovskite for Effective Bifunctional Oxygen Electrocatalysis in Alkaline Conditions. *Chem. Mater.* **2017**, *29*, 6228-6237.
16. Seh, Z. W.; Kibsgaard, J.; Dickens, C. F.; Chorkendorff, I.; Nørskov, J. K.; Jaramillo, T. F., Combining Theory and Experiment in Electrocatalysis: Insights Into Materials Design. *Science* **2017**, *355*.
17. Fabbri, E., et al., Dynamic Surface Self-Reconstruction Is the Key of Highly Active Perovskite Nano-Electrocatalysts for Water Splitting. *Nat. Mater.* **2017**, *16*, 925-931.
18. Kanan, M. W.; Nocera, D. G., In Situ Formation of an Oxygen-Evolving Catalyst in Neutral Water Containing Phosphate and Co^{2+}. *Science* **2008**, *321*, 1072-1075.
19. Kanan, M. W.; Yano, J.; Surendranath, Y.; Dincă, M.; Yachandra, V. K.; Nocera, D. G., Structure and Valency of a Cobalt−Phosphate Water Oxidation Catalyst Determined by in Situ X-ray Spectroscopy. *J. Am. Chem. Soc.* **2010**, *132*, 13692-13701.
20. González-Flores, D.; Sánchez, I.; Zaharieva, I.; Klingan, K.; Heidkamp, J.; Chernev, P.; Menezes, P. W.; Driess, M.; Dau, H.; Montero, M. L., Heterogeneous Water Oxidation: Surface Activity versus Amorphization Activation in Cobalt Phosphate Catalysts. *Angew. Chem., Int. Ed.* **2015**, *54*, 2472-2476.

21. Han, B.; Risch, M.; Lee, Y.-L.; Ling, C.; Jia, H.; Shao-Horn, Y., Activity and Stability Trends of Perovskite Oxides for Oxygen Evolution Catalysis at Neutral pH. *Phys. Chem. Chem. Phys.* **2015**, *17*, 22576-22580.
22. Seitz, L. C., et al., A Highly Active and Stable $IrO_x/SrIrO_3$ Catalyst for the Oxygen Evolution Reaction. *Science* **2016**, *353*, 1011-1014.
23. Moon, S. J., et al., Dimensionality-Controlled Insulator-Metal Transition and Correlated Metallic State in 5d Transition Metal Oxides $Sr_{n+1}Ir_nO_{3n+1}$ (n=1, 2, and ∞). *Phys. Rev. Lett.* **2008**, *101*, 226402.
24. Grimaud, A.; Diaz-Morales, O.; Han, B.; Hong, W. T.; Lee, Y.-L.; Giornado, L.; Stoerzinger, K. A.; Koper, M. T. M.; Shao-Horn, Y., Activating Lattice Oxygen Redox Reactions in Metal Oxides to Catalyse Oxygen Evolution. *Nat. Chem.* **2017**, *9*, 457-465.
25. Man, I. C.; Su, H.-Y.; Calle-Vallejo, F.; Hansen, H. A.; Martínez, J. I.; Inoglu, N. G.; Kitchin, J.; Jaramillo, T. F.; Nørskov, J. K.; Rossmeisl, J., Universality in Oxygen Evolution Electrocatalysis on Oxide Surfaces. *Chem. Cat. Chem.* **2011**, *3*, 1159-1165.
26. Rossmeisl, J.; Qu, Z. W.; Zhu, H.; Kroes, G. J.; Nørskov, J. K., Electrolysis of Water on Oxide Surfaces. *J. Electroanal. Chem.* **2007**, *607*, 83-89.
27. Mefford, J. T.; Hardin, W. G.; Dai, S.; Johnston, K. P.; Stevenson, K. J., Anion Charge Storage Through Oxygen Intercalation in $LaMnO_3$ Perovskite Pseudocapacitor Electrodes. *Nat. Mater.* **2014**, *13*, 726-732.
28. Nemudry, A.; Goldberg, E. L.; Aguirre, M.; Alario-Franco, M. A., Electrochemical Topotactic Oxidation of Nonstoichiometric Perovskites at Ambient Temperature. *Solid State Sci.* **2002**, *4*, 677-690.
29. Grenier, J. C.; Wattiaux, A.; Doumerc, J. P.; Dordor, P.; Fournes, L.; Chaminade, J. P.; Pouchard, M., Electrochemical Oxygen Intercalation into Oxide Networks. *J. Solid State Chem.* **1992**, *96*, 20-30.
30. Tahini, H. A.; Tan, X.; Schwingenschlögl, U.; Smith, S. C., Formation and Migration of Oxygen Vacancies in $SrCoO_3$ and Their Effect on Oxygen Evolution Reactions. *ACS Catal.* **2016**, *6*, 5565-5570.
31. Piovano, A.; Agostini, G.; Frenkel, A. I.; Bertier, T.; Prestipino, C.; Ceretti, M.; Paulus, W.; Lamberti, C., Time Resolved in Situ XAFS Study of the Electrochemical Oxygen Intercalation in $SrFeO_{2.5}$ Brownmillerite Structure: Comparison with the Homologous $SrCoO_{2.5}$ System. *J. Phys. Chem. C* **2011**, *115*, 1311-1322.
32. Paulus, W.; Schober, H.; Eibl, S.; Johnson, M.; Berthier, T.; Hernandez, O.; Ceretti, M.; Plazanet, M.; Conder, K.; Lamberti, C., Lattice Dynamics To Trigger Low Temperature Oxygen Mobility in Solid Oxide Ion Conductors. *J. Am. Chem. Soc.* **2008**, *130*, 16080-16085.
33. Galakhov, V. R.; Kurmaev, E. Z.; Kuepper, K.; Neumann, M.; McLeod, J. A.; Moewes, A.; Leonidov, I. A.; Kozhevnikov, V. L., Valence Band Structure and X-ray Spectra of Oxygen-Deficient Ferrites $SrFeO_x$. *J. Phys. Chem. C* **2010**, *114*, 5154-5159.
34. Lee, Y.-L.; Kleis, J.; Rossmeisl, J.; Morgan, D., *Ab Initio* Energetics of $LaBO_3$ (001) (B=Mn, Fe, Co, and Ni) for Solid Oxide Fuel Cell Cathodes. *Phys. Rev. B* **2009**, *80*, 224101.
35. Lee, Y.-L.; Kleis, J.; Rossmeisl, J.; Shao-Horn, Y.; Morgan, D., Prediction of Solid Oxide Fuel Cell Cathode Activity With First-Principles Descriptors. *Energ. Environ. Sci.* **2011**, *4*, 3966-3970.
36. Kresse, G.; Furthmüller, J., Efficient Iterative Schemes for Ab Initio Total-Energy Calculations Using a Plane-Wave Basis Set. *Phys. Rev. B* **1996**, *54*, 11169-11186.
37. Kresse, G.; Hafner, J., Ab Initio Molecular Dynamics for Liquid Metals. *Phys. Rev. B* **1993**, *47*, 558-561.
38. Blöchl, P. E., Projector Augmented-Wave Method. *Phys. Rev. B* **1994**, *50*, 17953-17979.
39. Perdew, J. P.; Burke, K.; Ernzerhof, M., Generalized Gradient Approximation Made Simple. *Phys. Rev. Lett.* **1996**, *77*, 3865-3868.
40. Schmidt, M.; Campbell, S. J., Crystal and Magnetic Structures of $Sr_2Fe_2O_5$ at Elevated Temperature. *J. Solid State Chem.* **2001**, *156*, 292-304.
41. Young, J.; Rondinelli, J. M., Crystal Structure and Electronic Properties of Bulk and Thin Film Brownmillerite Oxides. *Phys. Rev. B* **2015**, *92*, 174111.

42. Deganello, F.; Liotta, L. F.; Longo, A.; Casaletto, M. P.; Scopelliti, M., Cerium Effect on the Phase Structure, Phase Stability and Redox Properties of Ce-Doped Strontium Ferrates. *J. Solid State Chem.* **2006**, *179*, 3406-3419.
43. Muñoz, A.; de la Calle, C.; Alonso, J. A.; Botta, P. M.; Pardo, V.; Baldomir, D.; Rivas, J., Crystallographic and Magnetic Structure of $SrCoO_{2.5}$ Brownmillerite: Neutron Study Coupled With Band-Structure Calculations. *Phys. Rev. B* **2008**, *78*, 054404.
44. Suntivich, J.; Gasteiger, H. A.; Yabuuchi, N.; Shao-Horn, Y., Electrocatalytic Measurement Methodology of Oxide Catalysts Using a Thin-Film Rotating Disk Electrode. *J. Electrochem. Soc.* **2010**, *157*, B1263-B1268.
45. Wonders, A. H.; Housmans, T. H. M.; Rosca, V.; Koper, M. T. M., On-Line Mass Spectrometry System for Measurements at Single-Crystal Electrodes in Hanging Meniscus Configuration. *J. Appl. Electrochem.* **2006**, *36*, 1215-1221.
46. Wadati, H., et al., Hole-Doping-Induced Changes in the Electronic Structure of $La_{1-x}Sr_xFeO_3$: Soft X-Ray Photoemission and Absorption Study of Epitaxial Thin Films. *Phys. Rev. B* **2005**, *71*, 035108.
47. Lankhorst, M. H. R.; Bouwmeester, H. J. M.; Verweij, H., Thermodynamics and Transport of Ionic and Electronic Defects in Crystalline Oxides. *J. Am. Ceram. Soc.* **1997**, *80*, 2175-2198.
48. de Groot, F. M. F.; Grioni, M.; Fuggle, J. C.; Ghijsen, J.; Sawatzky, G. A.; Petersen, H., Oxygen 1s X-Ray-Absorption Edges of Transition-Metal Oxides. *Phys. Rev. B* **1989**, *40*, 5715-5723.
49. Karvonen, L.; Valkeapää, M.; Liu, R. S.; Chen, J. M.; Yamauchi, H.; Karppinen, M., O-*K* and Co-*L* XANES Study on Oxygen Intercalation in Perovskite $SrCoO_{3-\delta}$. *Chem. Mater.* **2010**, *22*, 70-76.
50. Abbate, M.; Zampieri, G.; Okamoto, J.; Fujimori, A.; Kawasaki, M.; Takano, M., X-Ray Absorption of the Negative Charge-Transfer Material $SrFe_{1-x}Co_xO_3$. *Phys. Rev. B* **2002**, *65*, 165120.
51. Mastrikov, Y. A.; Kuklja, M. M.; Kotomin, E. A.; Maier, J., First-Principles Modelling of Complex Perovskite $(Ba_{1-x}Sr_x)(Co_{1-y}Fe_y)O_{3-\delta}$ for Solid Oxide Fuel Cell and Gas Separation Membrane Applications. *Energ. Environ. Sci.* **2010**, *3*, 1544-1550.
52. She, S. X.; Yu, J.; Tang, W. Q.; Zhu, Y.; Chen, Y. B.; Sunarso, J.; Zhou, W.; Shao, Z., A Systematic Study of Oxygen Evolution Activity and Stability on La1-xSrxFeO3-δ Perovskite Electrocatalysts in Alkaline Media. *ACS Appl. Mater. Interfaces* **2018** (just accepted, DOI: 10.1021/acsami.8b00682).

TOC Graphic